Soft Matter

Strain localization and failure of disordered particle rafts with tunable ductility during tensile deformation

Journal:	*Soft Matter*
Manuscript ID	SM-ART-05-2020-000839.R1
Article Type:	Paper
Date Submitted by the Author:	17-Jul-2020
Complete List of Authors:	Xiao, Hongyi; University of Pennsylvania, Department of Physics and Astronomy Ivancic, Robert; University of Pennsylvania School of Arts and Sciences, Physics Durian, Douglas; University of Pennsylvania, Physics & Astronomy

Soft Matter

ARTICLE TYPE

Cite this: DOI: 00.0000/xxxxxxxxxx

Strain localization and failure of disordered particle rafts with tunable ductility during tensile deformation†

Hongyi Xiao,[a] Robert JS Ivancic,[a] and Douglas J Durian[a]*

Received Date
Accepted Date

DOI: 00.0000/xxxxxxxxxx

Quasi-static tensile experiments were performed for a model disordered solid consisting of a two-dimensional raft of polydisperse floating granular particles with capillary attractions. The ductility is tuned by controlling the capillary interaction range, which varies with the particle size. During the tensile tests, after an initial period of elastic deformation, strain localization occurs and leads to the formation of a shear band at which the pillar later fails. In this process, small particles with long-ranged interactions can endure large plastic deformations without forming significant voids, while large particles with short-range interactions fail dramatically by fracturing at small deformation. Particle-level structure was measured, and the strain-localized region was found to have higher structural anisotropy than the bulk. Local interactions between anisotropic sites and particle rearrangements were the main mechanisms driving strain localization and the subsequent failure, and significant differences of such interactions exist between ductile and brittle behaviors.

1 Introduction

Improving the ductility of disordered solids is an ongoing challenge as many of them have high application value but cannot withstand large plastic deformation beyond yielding, and often fail catastrophically.[1–4] Strain localization is an important process that leads to such failures, where strain in the early stage of deformation gradually localizes into a single region that spans across the sample.[5–7] This process often results in the formation of a shear band, where the material later fails. Strain localization and shear band formation occur in a variety of disordered solids, such as metallic glasses,[1,2] glassy polymers,[8,9] foams,[10,11] and granular materials,[12–14] despite the vast differences in the details of their composition. The similarity in their mechanical behavior comes from their disordered structures, which must rearrange during plastic deformation.[15] In a simplified picture for strain localization, early-stage local rearrangements tend to occur at sites that are structurally weak,[5,16,17] which in turn further increase their susceptibility for more rearrangements. It is believed that the cooperative effects of these local rearrangements can lead to the formation of a system-spanning shear band.[18–20] While there are several theoretical approaches that capture this process on continuum scale or mesoscale,[15,18,21,22] direct experimental observation of structural weakening is still lacking.

The structural evolution during strain localization and failure for materials with different ductility has not been well described. Although the occurrence of strain localization is universal, the pathway for it and the following failure process can be different. For example, materials like wet foams and bubble rafts can be highly ductile and exhibit a fluid-like behavior by sustaining large plastic deformation without forming significant voids or fractures.[11,23–25] Materials like metallic glasses and rocks can be highly brittle and form a sharp fracture after relatively little plastic deformation beyond yielding.[2–4] It is also possible to induce a brittle to ductile transition for a single type of material by tuning its properties such as temperature[8], particle shape,[4] internal friction,[26] preparation history,[8,27,28] system size,[29–33] and particle interaction.[8,26,34–36] The mechanisms leading to the differences in ductility are not entirely clear, but some of these methods modify particle properties, such as friction and shape, which suggests that the transition should have a microscopic origin. Thus the interaction between local structure and local dynamics could play an important role, and this can be better understood by examining a model experimental system with tunable ductility.

Here we focus on an approach to tune ductility used previously in simulations, which is to modify the interaction potential between particles.[8,34–36] These computational studies modified the Lennard-Jones potential and showed that the ductility of the disordered material increases with increasing the characteristic interaction range between particles. While this is relatively easy to accomplish in computer simulations, controlling interaction potential in an experimental system while tracking all the particles during the highly transient strain localization and failure processes is challenging. One relevant branch of experimental meth-

[a] Department of Physics and Astronomy, University of Pennsylvania, Philadelphia, PA 19104, USA * Email: djdurian@physics.upenn.edu

† Electronic Supplementary Information (ESI) available. See DOI: 10.1039/cXsm00000x/

ods is to fabricate disordered solids by connecting particles with tunable rigid bridges[37–40] By varying the stiffness and volume of these bridges, the fracture toughness of the material measured during crack propagation can be improved.[37,40] Although the underlying mechanism is more about the rigid bridges, rather than particle rearrangements, these results are encouraging for designing experiments with tunable particle interactions and preferably with more degrees of freedom for particles to rearrange.

Following this idea, we built and performed experiments on a model disordered solid made of a monolayer of granular particles floating at an air-oil interface (a particle raft) with capillary attractions between the particles, which is caused by the distortion a floating particle induces to the surrounding fluid interface. For a second particle that is nearby, this distortion causes an imbalance between its gravity, buoyancy, and the capillary force, which incurs a net attractive force between the two particles.[41–45] In this way, the capillary attraction is often long-ranged with the characteristic interaction range being the capillary length of the liquid involved, l_c,[41,44] which is roughly the size of the liquid meniscus around a particle. Combined with the short-ranged repulsion between particles in contact, the interaction potential shares similarities with potentials of other particles of interest such as atoms.[41] This similarity have made particle or bubble raft a model macroscopic system to study the physics of crystalline and amorphous materials.[46,47] Moreover, the viscous drag on the particles can be minimized by adjusting their velocities, so that the deformation can be free from basal friction,[48] which is often a problem for two-dimensional systems. The particle raft itself is also an important system in various fields such as self-assembly[49–51] and particle-coating for interfaces in applications including drug delivery and food production.[51–53] These applications can benefit from better understanding of mechanical behaviors of the particle rafts[25,47,54–58].

In this study, quasi-static tensile tests were performed for particle rafts and the capillary interactions were controlled by using different particle diameters, d, which essentially controls the characteristic interaction range in units of the particle diameter, l_c/d. This allowed us to observe structural changes of pillars showing different ductility, which qualitatively agrees with previous computational studies.[8,34–36] These experiments also reveal differences in the interplay between structure and dynamics during strain localization and failure for materials with different ductility.

The rest of this article is organized as follows. In Sec. 2, we describe the particle rafts, the experimental apparatus, and techniques for tracking particles and measuring the tensile force. Sec. 3 demonstrates the brittle and ductile behaviors observed in the experiments. Sec. 4 presents detailed analysis of structure-dynamics relations during strain localization and failure for pillars with different ductility. Sec. 5 presents the conclusions.

2 Tensile experiments of floating granular particles

In this study, the rafts consist of spherical particles floating at an air-oil interface. The particles are made of closed-cell Styrofoam with a density of approximately 15 kg/m^3. The particles are slightly polydisperse, and three batches of particles

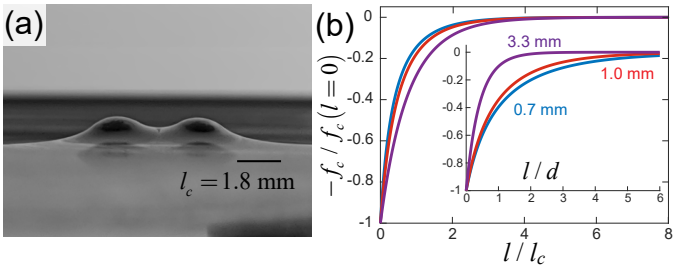

Fig. 1 Demonstration of the capillary interaction: (a) Photo of two similar sized floating $d = 3.3$ mm particles. (b) Analytical estimation[44] for the normalized capillary attraction of a single pair of particles vs. separation distance normalized by the capillary length or by the average particle diameter for the three particle sizes (inset).

with different mean diameters d were studied: $d = 0.7\pm0.1$ mm, $d = 1.0\pm0.1$ mm, and $d = 3.3\pm0.3$ mm, as measured using a Camsizer (Retsch). The oil used in the experiments is mineral oil as in a previous study.[59] The surface tension is estimated to be $\gamma = 27.4\pm0.7$ dyn/cm, the density is $\rho = 870\pm10$ kg/m^3, resulting in a capillary length of $l_c = \sqrt{\gamma/\rho g} = 1.8\pm0.2$ mm. The kinematic viscosity of the mineral oil is approximately ν =13.5 cSt.

An example of two floating particles is depicted in Fig. 1(a). As seen, the contact angle between the particle surface and the oil is small, and the particles are pulled down by the surface tension. This type of capillary attraction was recently analyzed by Dalbe *et al.*,[44] and the attractive force is $f_c = -CK_1[(l+d)/l_c]$. Here, l is the separation distance between the two particle surfaces ($l = 0$ at close contact), and $K_1(X)$ represents the modified Bessel function of the second kind and first order. The constant is defined as $C = \pi\gamma d sin(\phi_c)\tan^2(\phi_c+\theta)/K_1[d\sin(\phi_c)/2L_c]$, with θ being the contact angle and ϕ_c being an angle defined by the vertical position of the particles.[44] Thus, the order of magnitude of f_c is mainly determined by γd. Figure 1(b) shows how f_c (normalized by f_c at $l = 0$) decays with l (normalized by l_c). Here, the attraction decays rapidly over l_c and becomes negligible after $2l_c$. By normalizing l using d, the inset in Fig. 1(b) shows that f_c for the smaller particles (1.0 mm and 0.7 mm) can extend over a few d, while for the 3.3 mm particles f_c decays rapidly within one d. Thus, in units of d, the range of the capillary interaction increases with decreased particle diameter. Although the liquid surface distortion becomes much more complicated in a dense packing, resulting in many-body contributions to the potential energy, this difference in the interaction range should be preserved, at least over voids when a pair of particle are not completely blocked by other particles.[51]

The experimental apparatus used here is based on a previous setup designed to study plastic deformation of granular materials.[17,24,59–62] It is capable of applying a well-controlled global strain to a two-dimensional granular material while tracking all of the particle positions and measuring the global resistance force. In this study, this apparatus was adapted to performing tensile tests for the particle rafts, which is shown in Fig. 2(a). Here, a pillar of floating particles is sandwiched by two boundaries made of hollow carbon fiber tubes that also float on their own. The boundary on the bottom (of the picture) is fixed while the top

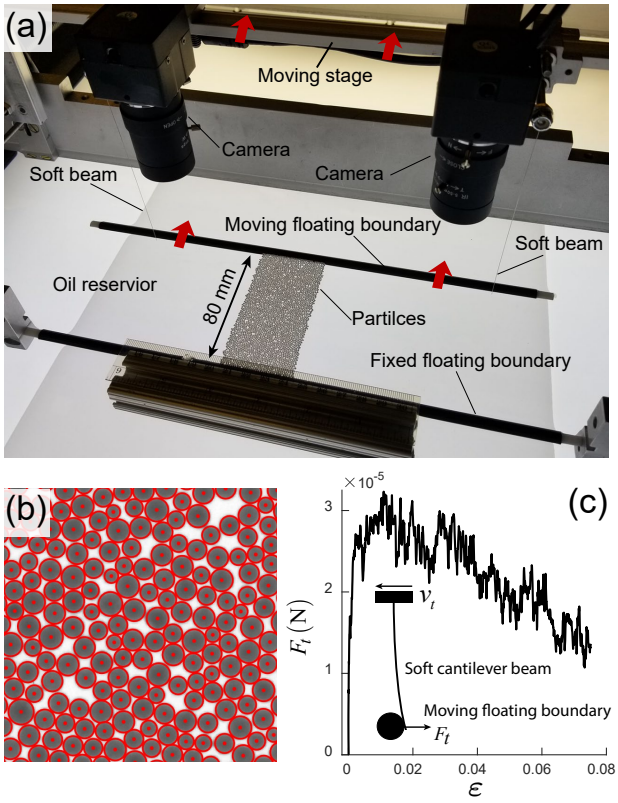

Fig. 2 The experimental apparatus. (a) A photo of the experimental apparatus. (b) An example of particle tracking with the tracked centers marked by dots and the tracked radii displayed using circles. (c) An example of measured tensile force vs. global strain for a single experiment with 1 mm particles.

boundary is driven away from the bottom boundary by a stage moving[24,61] at a constant tensile velocity v_t, which is conveyed via two soft cantilever beams that connect the moving stage and the top boundary. For the 0.7 mm and 1.0 mm particles, the particles are naturally attracted to the boundaries by the capillary attraction, which is stronger than the particle-particle attraction. For the 3.3 mm particles, the particle-boundary attraction is not as strong, so a layer of particles were glued to the boundary to prevent boundary detachment. The implementation of rigid boundaries suppresses deformation near the boundaries, which makes the deformation not rigorously uniaxial and bias deformation and failure towards the bulk region. In the analysis, we exclude the particles near the boundaries.

For studying local structure, it is important to prepare a well-shaped rectangular pillar made of a strictly single layer of densely packed particles. Here, we first initiated a thin pillar (less than $5d$ wide) that connected the two boundaries, and then we grew the pillar by dropping particles near its two sides, and let the particles assemble to the existing pillar driven by the capillary attraction, until the pillar reaches the desired shape. In this way, we can obtain dense disordered packing with no particle overlaps or large voids, see Fig. 2(a) and (b), and the fluctuation of the boundary shape is typically smaller than $1d$. Previous simulations of small-scale tensile tests suggest that the occurrence of strain localization and the formation of the shear band is not sensitive to the system size as long as it is larger than 3-4 times of the shear band size.[32] We also found that shear band formation is not sensitive to the system size when the pillar height is larger than approximately $40d$. The height/width ratio was varied from 1:1 to 4:1 and it does not qualitatively influence shear banding. Thus, a reasonable pillar size was chosen to be $L_0 = 80d$ in height and $W_0 = 40d$ in width for all the particle sizes. We chose a tensile strain rate of $\dot{\varepsilon} = v_t/L_0 = 1.3\times10^{-5}$ s^{-1} for all the particle sizes, corresponding to $v_t = 1.04\times10^{-3}$ d/s. This results in a capillary number of $Ca = \mu v_t/\gamma$ that is on the order of 10^{-6}, where $\mu = \nu\rho$, and a Reynolds number of $Re = v_t d/\nu$ that is on the order of 10^{-4}. This suggests that hydrodynamic forces and viscous forces are much smaller than the capillary attractions in the system, and the experiments were in a quasi-static regime.

For each experiment, images with a resolution of 2048×2048 px^2 were recorded by a JAI/Pulnix TM-4200CL camera with a time interval of 0.75 s, corresponding to a displacement of the moving boundary of $7.8\times10^{-4}d$. The positions and radii of all the particles were tracked using a previously developed algorithm with a sub-pixel accuracy,[24,61] and examples of the tracked particle center and diameter are plotted on top of a raw experimental image in Fig. 2(b). To reduce noise, we further applied a Gaussian filter to the measured positions with a time window corresponding to a moving boundary displacement of approximately $1/15d$, similar to our previous work.[24,24] And then particle velocities, $\mathbf{v}$, were calculated based on the filtered positions.

The global tensile force, F_t, was also measured during the experiment, which ranges from 10^{-6} to 10^{-3} N and is too small for typical commercial sensors. Instead, F_t was determined by measuring the deflection that the soft cantilever beams experienced while pushing on the moving boundary, see Fig. 2(c). The deflection is linear to F_t[63] and it was measured as the relative displacement between the boundary and the moving stage. This displacement was monitored using two webcams mounted on the stage (Fig. 2(a)), with a resolution of approximately 90 px/mm and a time interval of 5.8 s. The beams are made of stainless steel, and the stiffness of the beams were chosen so that observable deflections can be generated, with the maximum deflection being slightly below 1 mm. The beam stiffness was separately calibrated using a commercial 10 g force sensor (Transducer Techniques). As demonstrated in Fig. 2(c), the result captures the trend of F_t including its sharp initial increase. The major source of error comes from possible variation of the beam length between the calibration and the experiment due to mounting. This could induce an error in the conversion from deflection to force that is within 5%, while not influencing the shape of the loading curve.

For each particle size, 50 tensile deformation tests were performed to achieve good statistics on local deformation and structural changes, as discussed in the following sections.

3 Observations of brittle and ductile behaviors

In the tensile experiments, a transition from brittle to ductile behavior occurs as the particle size decreases. To visualize the transition, we quantify the local deviatoric strain rate, J_2, in the deforming pillar at different global strains. The calculation of J_2 is

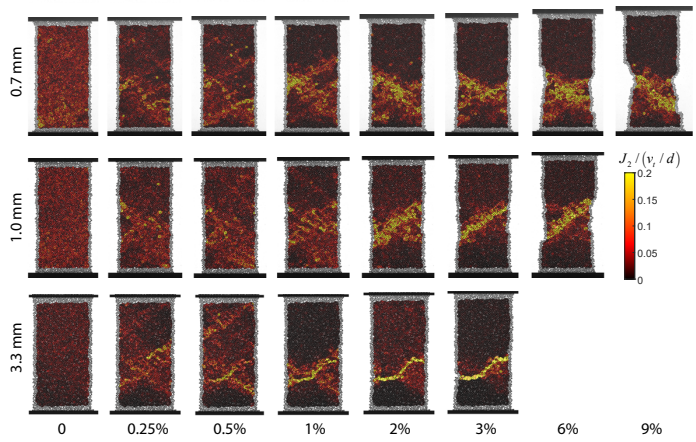

Fig. 3 Normalized J_2 for examples of different particle sizes at different global strains. In each pillar, local J_2 for each triangle is plotted on top of the original experimental image. See the supplementary material for videos of the three experiments.

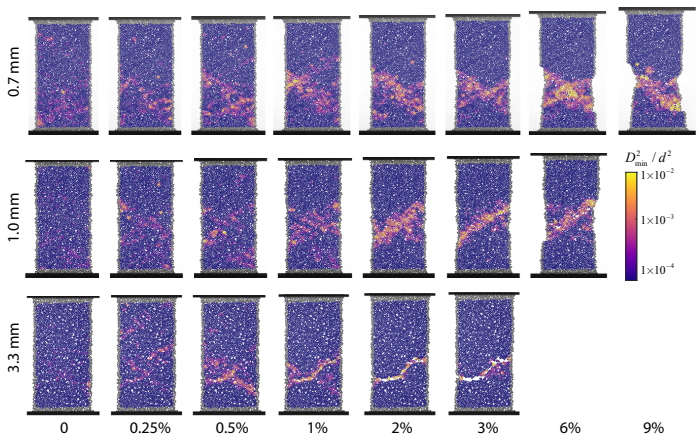

Fig. 4 Normalized D^2_{min} for examples of different particle sizes at different global strains (same cases as Fig.3). In each pillar, the particles are colored by their D^2_{min} values. See the supplementary material for videos of the three experiments.

detailed in our previous studies,[24,62] which is based on Delaunay triangulation of instantaneous particle positions. For a single triangle, we calculated a local strain rate tensor $\dot{\boldsymbol{\varepsilon}}$ based on the velocity $\mathbf{v}$ of the particles on its vertices using the constant strain triangle formalism,[64]

$$\begin{pmatrix} v_x(x,y)-v_{x,c} \\ v_y(x,y)-v_{y,c} \end{pmatrix} = \begin{pmatrix} \dot{\varepsilon}_{11} & \dot{\varepsilon}_{12} \\ \dot{\varepsilon}_{21} & \dot{\varepsilon}_{22} \end{pmatrix} \begin{pmatrix} x \\ y \end{pmatrix}, \tag{1}$$

where x and y are Cartesian coordinates relative to the triangle centroid, and $v_{x,c}$ and $v_{y,c}$ are the velocity at the centroid (to be computed). From the symmetric portion $\dot{\varepsilon} = (\dot{e}_{ij}+\dot{e}_{ji})/2$ we calculate the local deviatoric strain rate J_2,

$$J_2 = \frac{1}{2}\sqrt{(\dot{\varepsilon}_{11}-\dot{\varepsilon}_{22})^2+4\dot{\varepsilon}_{12}^2}. \tag{2}$$

Following our previous work,[24,62] we normalize J_2 by a characteristic strain rate v_t/d in the analysis.[24]

While J_2 is good for identifying deviatoric deformation, we also calculated a second local quantity, D^2_{min}, which specifically picks out the non-affine part of the deformation that corresponds to local particle rearrangements.[15] The calculation of D^2_{min} is based on the change of particle positions, $\mathbf{r}_i$, between two consecutive frames within a time interval of Δt. For each particle i, a best-fit local affine deformation matrix, $\mathbf{E}$, can be computed, and then the non-affine displacement, D^2_{min}, associated with particle i can be calculated,[21,60,65]

$$D^2_{min,i}(t,\Delta t) = \frac{1}{n}\sum_{i=1}^{n}\left|\mathbf{r}_{ji}(t+\Delta t)-\mathbf{E}\mathbf{r}_{ji}(t)\right|^2, \tag{3}$$

where $\mathbf{r}_{ji} = \mathbf{r}_j - \mathbf{r}_i$ is the relative position between particle i and its neighbor j. Here we selected a time interval that corresponds to a global tensile strain of 0.2%, which is a duration that is large enough to capture a clear signal of non-affine displacement. The search radius for neighbors is set to be $1.25d$ so that the first shell of neighbors is included, which is roughly the same group of particles that share triangles with the center particle. We then normalize D^2_{min} by d^2.[60,65] Using J_2 and D^2_{min}, we demonstrate examples of strain localization and failure for the three particle sizes at different global strains, $\varepsilon = (L-L_0)/L_0$, where L is the instantaneous pillar height. These results are shown in Figs. 3 and 4, where triangles colored by J_2 or particles colored by D^2_{min} are plotted on top of experimental images. Note that the particles near the four boundaries are left out of the analysis of J_2 and D^2_{min}.

Figures 3 and 4 show that while strain localization and failure occur for all particle sizes, qualitative differences exist. At the beginning ($\varepsilon \approx 0$), the local J_2 is uniformly distributed for all d, and little rearrangement occurs, indicating initial elastic deformation. The magnitude of J_2 decreases slightly with increased d. As ε proceeds to 0.25% and 0.5%, J_2 is still fairly spread out in the pillar, but its distribution is clearly non-uniform. This hint of strain localization is accompanied by the appearance of some high D^2_{min} values at locations where J_2 is also higher. The difference for the three particle sizes is small, but starts to show up as ε increases to around 1%. Now, the deformation for the 3.3 mm case is strongly localized to a single region, evident by a narrow and system-spanning band with high J_2. However, for the 0.7 mm and 1.0 mm cases, J_2 is distributed in a relatively wider region, and J_2 gradually concentrates into a system-spanning band as ε approaches 2%. In the meantime, D^2_{min} in the bands for the smaller particles is higher and has a wider spread comparing to that of the 3.3 mm particles, indicating that the smaller particles are more capable of rearranging.

The emergence of the strain-localized region can be treated as the onset of failure. As ε further increases, a significant difference in the ductility of the pillars appears. For the 3.3 mm particles, a fracture develops from the strain-localized region and can be observed at $\varepsilon = 2\%$ and 3%. At this point, the high J_2 at the fracture is mainly due to the growth of voids, which are visible as the white spaces between particles in the D^2_{min}. The pillar breaks apart with little deformation, showing typical a brittle behavior.

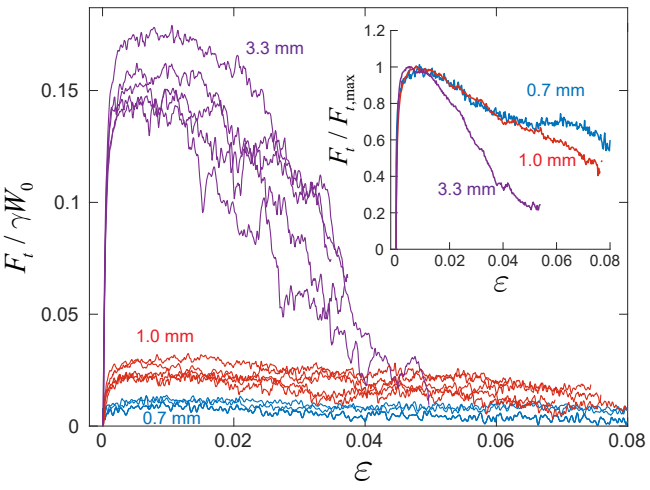

Fig. 5 Normalized stress-strain curves measured from individual experiments. Five cases are shown for each particle size. Inset: tensile force averaged over 50 experiments for each particle size, which is then normalized by the maximum average tensile force, $F_{t,max}$.

For 0.7 mm particles, rearrangements occur over extended region of the sample (at $\varepsilon = 3-9\%$), and no significant system-spanning fracture exists. Instead, a long-lasting shear occurs between the upper and lower half of the pillar divided by the strain-localized region, which is a shear band. The overall shape of the pillar deforms significantly and the shear band length shortens as ε increases, showing a typical ductile behavior. The failure of 1.0 mm particles is close to that of 0.7 mm particles, but by examining all 50 runs, we found there are typically a few voids growing at large ε, similar to the 3.3 mm particles.

Throughout all experiments, strain localization and failure are consistent with Figs. 3 and 4. For each particle size, the shear band appears at similar global strains with similar characteristics, while its vertical location varies. The average angle of the shear band with the horizontal direction is 26.3±5.2° for $d = 0.7$ mm, 27.5±4.3° for $d = 1.0$ mm, and 26.6±6.9° for $d = 3.3$ mm. Note that for the 3.3 mm particles, the failure planes still have the same inclination as that for the smaller particles, which could arise from similarities in their early-stage deformation, so we also refer to them as shear bands. The value of this inclination is different from the 45° that is commonly seen in materials like metallic glasses and polymers.[1,2,8,9] The deviation is possibly a result of particle friction that is unique to granular materials.[6,66] This could be explained as a combined effect of a local Mohr-Coulomb failure criterion and long-range elastic interactions between the failure sites (local rearrangements).[19]

Another way to examine the brittle-to-ductile transition is to study the stress-strain curves. Here, we calculate the global tensile stress by normalizing the measured tensile force F_t with γW_0, which can be understood as the characteristic magnitude of the pairwise capillary attraction force, γd,[44] times the number of particles across the width, W_0/d. The result of this straightforward normalization is shown in Fig. 5, with five individual measurements demonstrated for each particle size. The maximum stress increases with d, which is possibly due to the fact that larger particles can bring larger distortion to the liquid surface and thus have larger capillary attractions.[44] The stress difference is comparable to the difference in their Bond number, $Bo = d^2/4l_c^2$, which compares gravitational forces with the capillary forces. Although differences exist between individual experiments, the results show a significant change in ductility with particle size.

Initially, an elastic behavior is observed for all d with the tensile stress rapidly increases, agreeing with the J_2 and D^2_{min} results. For ε =0.25%-1%, the increase of the tensile stress slows down until it flattens, which coincides well with the starting of strain localization, indicating plastic deformation beyond yielding. The third period is the failure process evident by the decay of stress. A distribution of of maximum stress and ductility can be found in the individual measurements, which is likely due to different initial structure. To show the difference in ductility more clearly, we first average the tensile stress over the 50 experiments for each d, and then normalize it by the maximum average tensile stress, which gives $F_t/F_{t,max}$ (Fig. 5 inset). This normalization shows a clear trend that the rate of decay is slower for smaller particles, which further confirms their higher ductility. The relatively rapid decay of strength for the 3.3 mm particles is mainly due to the growth and merging of voids, while the slower decay of strength for the 0.7 m is mainly due to the decrease of cross-sectional area. The strength decay of the 1.0 mm particles is intermediate in a way that it follows the curve of the more ductile 0.7 mm particles until approximately $\varepsilon = 5\%$, and falls off, which could be an effect of void growth.

These results show that we experimentally achieved a brittle-to-ductile transition by decreasing d, which corresponds to increasing the interaction range of the capillary attraction. This transition agrees qualitatively with transitions found in previous numerical simulations that modified Lennard-Jones-like potentials.[8,34–36]

4 Structural changes during strain localization and failure

4.1 Quantifying structural changes

In this section, we quantify structural changes during tensile deformation by examining the local structural anisotropy and study how it interacts with local deformation. The structural anisotropy can be quantified using different approaches, such as free volume,[67] Voronoi cell size and shape,[68,69] local topology,[70] and machine learning.[17,71] For this study, we focus on a quantity that, like J_2, is defined over Delaunay triangles: The area-weighted divergence of the particle center-to-Voronoi cell centroid vector field, Q_k,[72]

$$Q_k = \nabla \cdot \mathbf{C}_k \frac{A_k}{\langle A \rangle}. \quad (4)$$

For a Delaunay triangle k, C_k is the vector field pointing from particle centers to the centroid of corresponding Voronoi cells, A_k is the area of the triangle, and $\langle A \rangle$ is the average area of all triangles. An example of calculated Q_k field is shown in the inset of Fig. 6, along with the corresponding triangles and C_k field. By construction, the average Q_k over an entire packing is zero. Positive values of Q_k tend to correspond to closely packed, or

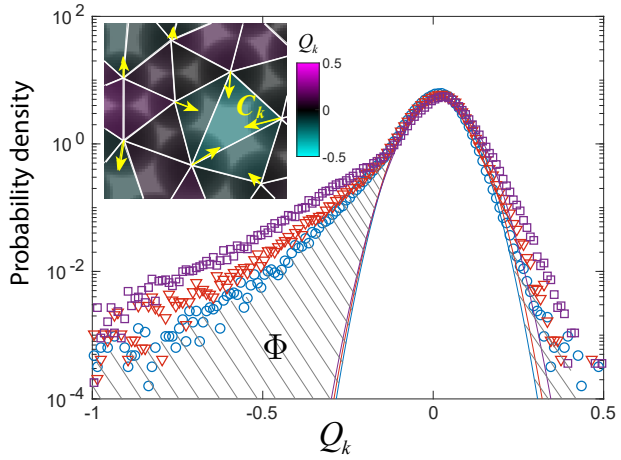

Fig. 6 Initial Q_K distribution calculated using 50 experiments for $d = 0.7$ mm (blue circles), $d = 1.0$ mm (orange triangles), and $d = 3.3$ mm (purple squares). The curves are Gaussian fits to the region $-0.15 < Q_k < 0.15$ for the three sizes and are colored accordingly. Shaded area represent Φ for $d = 0.7$ mm particles. Inset demonstrate Q_k calculated based on Delaunay triangles (with white edges) and the vector field C_k (yellow arrows).

"overpacked," sites, while negative values correspond to voids, or "underpacked," sites. The distribution of Q_k value was previously observed to be nearly Gaussian except for a noticeable tail of underpacked regions.[72] Videos of experiments with particles colored by their Q_k values can be found in the supplementary materials, along with videos for J_2 and D^2_{min}.

Figure 6 shows the initial Q_k distribution calculated using initial particle positions for each d. Here, triangles connecting boundary particles are again not included. The majority of Q_k resides in the region around zero with a Gaussian-like distribution,[24,62,72] which is made clear by plotting a Gaussian fit calculated using $-0.15 < Q_k < 0.15$ for each particle size. For $Q_k < -0.15$, the distribution deviates from Gaussian and becomes exponential-like instead, corresponding to the existence of highly underpacked sites. For this tail, the decay of the probability density is slower for larger d, meaning that the portion of highly underpacked sites is larger for more brittle materials. The tails in the Q_k distributions for $Q_k > 0.15$ also deviate from the Gaussian fits following a similar trend. Note that these pillars are prepared following the same procedure and the initial packing fraction is similar for the three sizes, which is 0.77±0.01 for 0.7 mm, 0.78±0.01 for 1.0 mm, and 0.77±0.01 for 3.3 mm (averaged over 50 experiments). The difference in the shape of the tails should come from the way particles assemble into the pillar during the preparation, which is again dictated by their capillary attraction.

Previous studies suggest that the distribution of Q_k is related to important physics in disordered solids including jamming transition,[72] structural strength,[24] and shear band formation.[62] To study the significance of structure during strain localization, we quantify the tails in the distribution by measuring the area difference between the probability density of Q_k distribution, $p(Q_k)$, and the corresponding Gaussian fit, $p_G(Q_k)$, which is the shaded

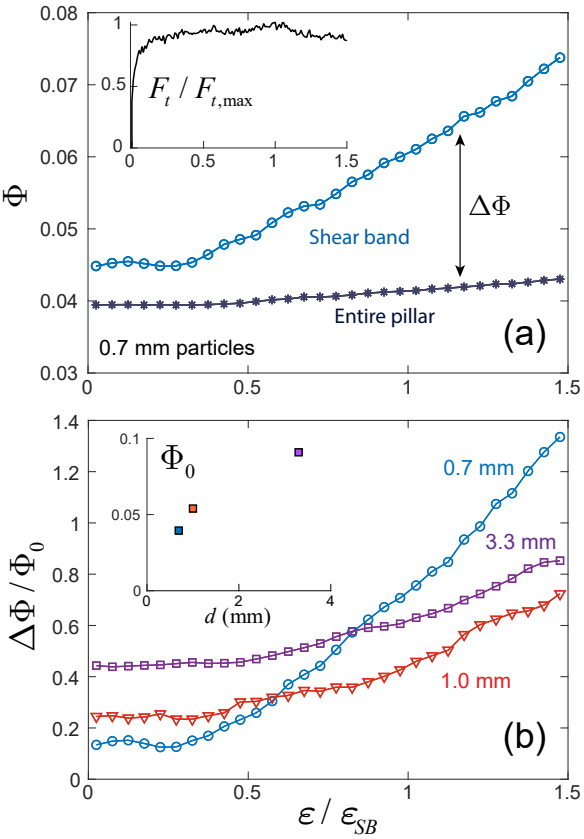

Fig. 7 Excess portion Φ calculated from the Q_k distribution. (a) Φ vs. $\varepsilon/\varepsilon_{SB}$ calculated for the entire pillar (dark asterisks) and for the shear band region only (blue circles), for $d = 0.7$ mm. Inset shows averaged $F_t/F_{t,max}$ vs. $\varepsilon/\varepsilon_{SB}$. (b) $\Delta\Phi/\Phi_0$ vs. $\varepsilon/\varepsilon_{SB}$ calculated for $d = 0.7$ mm (blue circles), $d = 1.0$ mm (orange triangles), and $d = 3.3$ mm (purple squares). Inset shows initial Φ_0 vs. d.

area in Fig. 6, in a linear scale. We refer to it as the excess area, Φ, and it is calculated as

$$\Phi = \int_{-\infty}^{Q_k^-} (p(Q_k) - p_G(Q_k))\, dQ_k + \int_{Q_k^+}^{\infty} (p(Q_k) - p_G(Q_k))\, dQ_k, \quad (5)$$

where the integration limits are, $Q_k^- = -0.15$ and $Q_k^+ = 0.15$ for all d, which correspond to where $p(Q_k)$ starts deviating from $p_G(Q_k)$. In Fig. 7, we study how Φ changes as the global tensile strain increases. Here, we first normalize the global strain, ε, by the strain when the shear band appears, ε_{SB}, which is set to be the strain when the measured tensile force starts to decay. The average ε_{SB} over 50 experiments is 1.3±0.4% for 0.7 mm particles, 1.2±0.4% for 1.0 mm particles, and 1.0±0.3% for 3.3 mm particles. Figure 7(a) shows Φ vs. $\varepsilon/\varepsilon_{SB}$ averaged over 50 experiments for 0.7 mm particles as an example. In addition, we also show the change of the normalized tensile stress, $F_t/F_{t,max}$, vs. $\varepsilon/\varepsilon_{SB}$ in the inset of Fig. 7(a).

Here, we examine Φ calculated using only triangles in the region that would develop into a shear band and compare it to Φ for the entire pillar. For the shear band, we collect triangles that are connected to particles within $1.5d$ distance to the center plane of the shear band. This narrow distance threshold allows us to pick

up strong structural signals in the early stage of the deformation. The results are not sensitive to this threshold or the integration limits in Eq. 5. The comparison in Fig. 7(a) shows that Φ in the shear band region is initially higher, indicating that strain localization favors locations with higher anisotropy. In the elastic period ($\varepsilon/\varepsilon_{SB}<0.3$), Φ remains relatively unchanged, indicating little structural change during elastic deformation while the tensile stress quickly builds up. For $\varepsilon/\varepsilon_{SB} > 0.3$, as the pillar enters the plastic regime with initiation of rearrangements and strain localization, Φ in the shear band region starts to increase at a rate that is much faster than the rate for the bulk. This increase coincides well with the appearance of local rearrangements, suggesting a strong structure-dynamics coupling. No significant transition of Φ is found at $\varepsilon/\varepsilon_{SB} = 1$, indicating that the structure change during the initiation of the shear band is rather smooth, and indeed no sharp stress drop is observed in the force measurements (Fig. 5).

Figure 7(b) shows the difference in Φ between the shear band region and the bulk, $\Delta\Phi$, which is normalized by the initial access area of the bulk, Φ_0 (shown in the inset). For all particle sizes, $\Delta\Phi/\Phi_0$ is initially higher, and it is larger for larger d. For all three sizes, $\Delta\Phi/\Phi_0$ also experiences a relatively unchanged interval during elastic deformation, before it starts to increase at a global strain that coincides well with strain localization. *Thus, there is a strong structural signal in the strain localization process that exists long before the shear band actually appears, and it is magnified by plastic rearrangements in the early stage of the deformation.* The higher initial structural anisotropy in the shear band region is reminiscent of our previous computational study of pulled polymer nanopillars where the location of the shear band can be predicted with high accuracy using the initial structural information,[9] indicating that structural difference is a universal factor that drives strain localization of disordered solids. Figure 7(b) also shows that both Φ_0 and $\Delta\Phi/\Phi_0$ are higher for more brittle systems, indicating possible influences of the initial structure on ductility. The implications of the structural difference in the Q_k distribution will be interpreted by particle-level relations between rearrangements and local deformation in the following subsection.

4.2 Structure-dynamic relations during strain localization

To examine local relations between structural anisotropy and local deformation, we bin the deviatoric strain rate, J_2, of a triangle according to its Q_k value, and average over all triangles within each bin.[24,62] The bin-averaged J_2–Q_k relation during plastic deformation often has a "V-shape", where J_2 is high at highly positive and highly negative Q_k, and low around $Q_k = 0$.[24,62] Different from our previous experiments with a frictional substrate leading to highly localized plastic deformations,[24,62] a well defined elastic regime exists here. This motivated us to compute the relation at different ε which are shown for the 0.7 mm particles as an example in Fig. 8(a). Here, we focus on the range of Q_k where we have ample amount of data, and we normalize the bin-averaged J_2 by the average J_2 of all triangles at a specific $\varepsilon/\varepsilon_{SB}$, which is $\langle J_2\rangle$. In the initial elastic regime at small $\varepsilon/\varepsilon_{SB}$, J_2–Q_k relation is indeed different from the "V-shape" relation. Instead, J_2 is lowest at the smallest Q_k and increases linearly with Q_k, especially for the very beginning (light-colored). The "V-shape" relation is recovered in the period dominated by plastic rearrangement, and the transition appears gradual. This is a dynamic-structure signature of the yield transition, another signal that coincides with strain localization.

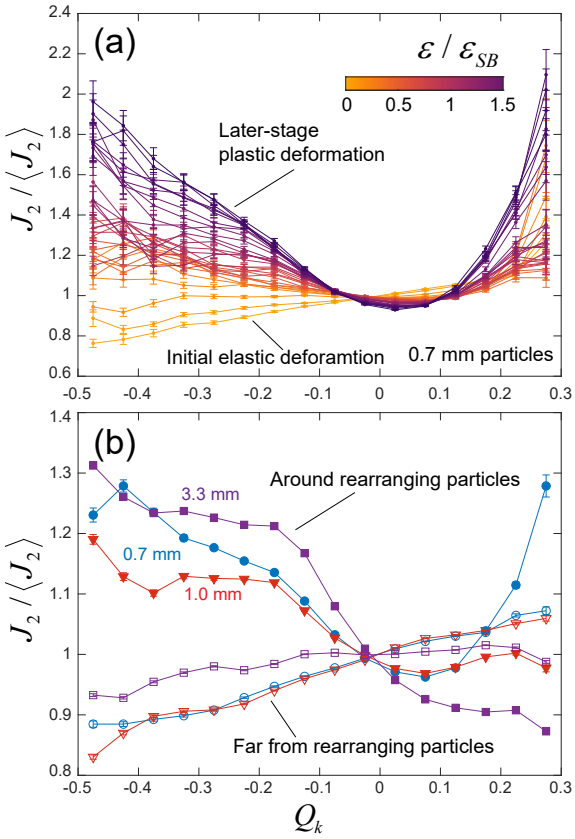

Fig. 8 Relations between structure and local deviatoric deformation. (a) Triangle J_2 averaged by binning according to their Q_k values for $d = 0.7$ mm particles at different global strains. All triangles in the pillar are used and $\langle J_2\rangle$ is their average at each global strain. (b) $J_2/\langle J_2\rangle$ vs. Q_k calculated for triangles around rearranging particles (closed) and far from rearranging particles (open) for for $d = 0.7$ mm (blue circles), $d = 1.0$ mm (orange triangles), and $d = 3.3$ mm (purple squares). Error bars represent standard errors in both plots.

The difference in the J_2–Q_k relation comes from the composition of the deformation: in the elastic period, J_2 is dominated by affine deformation, while in the later stage, J_2 is dominated by plastic rearrangements. To further investigate this difference, we compute the J_2–Q_k relation in a second way. Instead of using triangles at a specific $\varepsilon/\varepsilon_{SB}$, we include all triangles collected within $0 < \varepsilon/\varepsilon_{SB} < 1$ and separate them into two groups: the ones that are near rearranging particles, and the ones far away from rearranging particles. Here we consider a particle rearranging when its $D^2_{min}/d^2 > 1\times10^{-4}$, a rather low threshold to make sure that we filter out all significant rearrangements and get truly affine deformation. We consider a triangle to be far away from a rearranging particle if it is not connected to either this particle or its first shell of neighbors (*i.e.*, two layers away), and vice versa.

The calculated J_2–Q_k relations are shown in Fig. 8(b) for all d,

which show a clear difference between affine elastic deformation and plastic rearrangements. For triangles far away from rearrangements, the J_2–Q_k relations show a linear increase of J_2 with Q_k, consistent with the early-stage results in Fig. 8(a), confirming that it is indeed a dynamic-structure signature for elastic deformation. A possible explanation for J_2 being higher for more overpacked sites is that the capillary attractions for closer particles are stronger, so that these sites have higher local elastic moduli and bear more elastic loading in a heterogeneous force network.

Plastic rearrangements favor highly anisotropic sites, especially for highly underpacked sites with negative Q_k.[24,62] This is evident in the results for triangles around rearrangements, which agree with the later-stage relations in Fig. 8(a). The rise of J_2 in the overpacked side ($Q_k > 0$) of the "V-shape" is more significant for smaller d (more ductile). For the 3.3 mm particles that have the shortest interaction range, it is possible that the strength of a compact triangle is too strong for it to rearrange. In our previous studies of compression and penetration for particles of different shapes, dimers showed a substantially higher strength and poor ability to rearrange due to interlocking,[24,62] and do not have the upturn in the J_2–Q_k relation. This similarity indicates that the upturn in the positive Q_k side can serve as a signature for the degree of ease for rearranging, and thus their ductility. The lack of rearranging capability for highly overpacked sites could also contribute to the higher tensile stress for larger particles, as there is often a trade-off between strength and ductility during such transitions.[8] In general, this preference for rearrangements to occur at highly structural anisotropic sites means that the increase of Φ can be considered as accumulation of structural damage[18,33] during plastic deformation, which eventually leads to strain localization and failure.

4.3 Structure-dynamic relations during failure

Finally, we explore the structure-dynamic relation during failure, which greatly influences the ductility. At this period, while Q_k is still a proper quantity for studying the structure-dynamic relation and identify growing voids (with highly negative Q_k), we choose to directly use the triangle area, A_k, to represent the local structure, since it can be compared to important length scales such as d and l_c. For the choice of a quantity representing the dynamics where void growth is important, we use the volumetric strain rate, $\dot{\varepsilon}_v = \dot{\varepsilon}_{11} + \dot{\varepsilon}_{22}$, and also normalize it by v_t/d. The late stage of deformation, $\varepsilon > \varepsilon_{SB}$, is highly localized and all large rearrangements is confined in the failure region (Fig. 4). Thus, we focus on triangles in this region, which can be found by selecting triangles around particles with high D^2_{min}. We set the threshold to be $D^2_{min}/d^2 > 1 \times 10^{-3}$ and the search radius to be two layers around these particles so that roughly all triangles in this zone are included.

The structure-dynamics relation between the triangle areas and the volumetric strain rate is shown in Fig. 9. For each particle size, we bin $\dot{\varepsilon}_v/(v_t/d)$ by A_k/d^2 and show the bin-averaged values in Fig. 9(a). The results show that the averaged $\dot{\varepsilon}_v/(v_t/d)$ is positive, and triangles with larger areas tend to have larger volumetric strain rates. This trend works in favor of the growth of larger

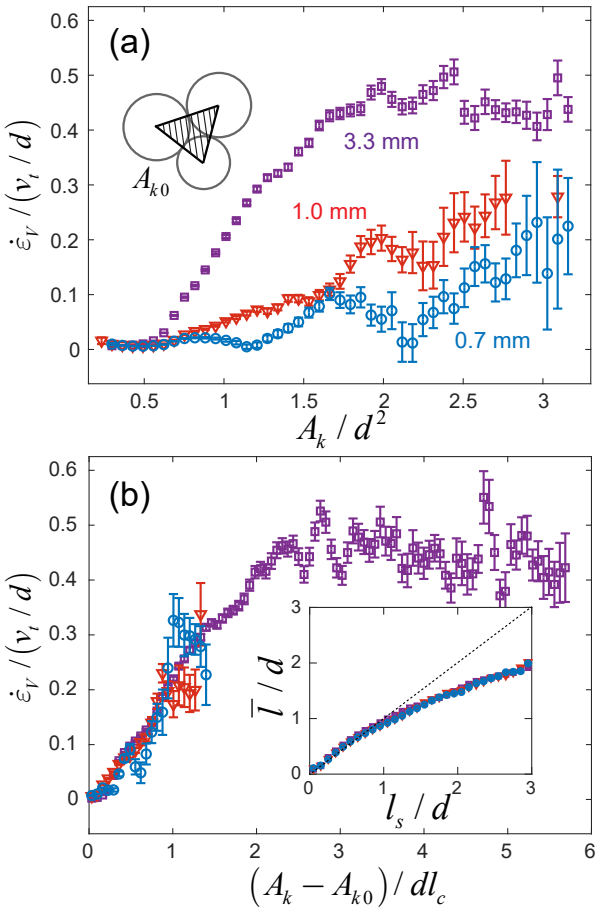

Fig. 9 Structure-dynamic relation during failure. (a) Normalized triangle volumetric strain rate, $\dot{\varepsilon}_v/(v_t/d)$, averaged by binning according to their normalized areas, A_k/d^2. (b) $\dot{\varepsilon}_v/(v_t/d)$ binned according to $(A_k - A_{k0})/dl_c$. Inset: the average pairwise separation distance $\bar{l}/d$ vs. l_s/d for the three particle sizes. In all plots, error bars represent standard errors and symbols are blue circles for $d = 0.7$ mm, orange triangles for $d = 1.0$ mm, and purple squares for $d = 3.3$ mm.

voids during failure, and the differential growth rate of A_k can further increase the local packing anisotropy, which is consistent with the Q_k-based measure in Fig. 7. Moreover, the increase rate of $\dot{\varepsilon}_v/(v_t/d)$ with A_k/d^2 is significantly larger for larger particles, showing that the void growth for brittle failure is more dramatic. For ductile failure, while $\dot{\varepsilon}_v/(v_t/d)$ for the 0.7 mm particles is relatively low, the deviatoric strain rate J_2 can actually be higher than J_2 for the brittle materials, see Fig. 3. These results quantitatively show that ductile materials can have larger-scale particle rearrangements while avoiding any significant void growth during failure.

The initial plateau at small A_k/d^2 in Fig. 9(a) corresponds to the regime where particles are in close contact. The plateau exists because A_k/d^2 at close contact is not a unique value due to the polydispersity of the particle diameters. To correct this, we subtract the triangle area corresponding to close contact, A_{k0}, which is calculated using the actual diameter of the constituting particles, as sketched in Fig. 9(a). In this way, $A_k - A_{k0}$ is the actual area that corresponds to the separation of particles for a trian-

gle. Upon further examination, we found that the increase rate of $\dot{\varepsilon}_v/(v_t/d)$ with $(A_k - A_{k0})/d^2$ is proportional to d, which motivated us to scale $(A_k - A_{k0})/d^2$ by l_c/d. Figure 9(b) shows the results of $\dot{\varepsilon}_v/(v_t/d)$ that is bin-averaged according to $(A_k - A_{k0})/dl_c$. In this way, data for the three particle sizes collapses, showing a linear initial increase followed by a plateau at large areas.

One way to rationalize this new scaling is that during tensile deformation, the triangles mainly expand in one direction, while the separation in the other direction remains at a characteristic length of d. Thus $(A_k - A_{k0})/d$ gives a length scale for the separation in the expanding direction, l_s, which can be compared to l_c. Within $l_s/l_c \approx 2$, the increase of l_s results in faster expansion. The upper limit, $l_s/l_c \approx 2$, somehow agrees with the decay range of the capillary attraction f_c as shown in Fig. 1(b). The inset in Fig. 9(b) shows how l_s compares with the normalized average pairwise separation distance of the triangle particles, $\bar{l}/d$. The results show that l_s is comparable to $\bar{l}$ in magnitude, which confirms that l_s is comparable to l in Fig. 1(b). For $l_s/l_c > 2$, a second regime is reached where $\dot{\varepsilon}_v$ is roughly proportional to v_t/d, and l_s/l_c no longer has an influence over it, suggesting that the particles have broken free from the capillary attraction. This plateau in the volumetric strain rate means that the area increase rate, dA_k/dt, is proportional to A_k, indicating an exponential growth, a rather drastic growth mode that facilitates failure. Only the 3.3 mm particles reaches this regime, which distinguishes brittle and ductile failure. This scaling reveals how ductility is tuned by the interaction range l_c/d at the particle level. Experimenting at larger systems might allow larger voids to form for smaller particles and eventually reach the plateau, and possibly trigger a system-size induced ductile-to-brittle transition.[29–33]

5 Conclusions

We have shown that a model disordered solid made of a particle raft can experience elastic deformation, strain localization, and failure during quasi-static tensile tests. The ductility of the material can be tuned by using different particle sizes, which in turn controls the interaction range for the capillary attractions. Smaller particles with longer interaction ranges are more ductile and can endure larger global tensile deformation without forming larger voids and fractures. Larger particles with shorter interaction ranges fail in a brittle way with a fracture forming after relatively small global tensile deformation.

Distinct local structure-dynamic relations were found between elastic deformation and plastic rearrangements, with the latter being responsible for inducing structural changes and strain localization. The excess portion of local sites with high structural anisotropy was found to be higher for strain localized regions and also for more brittle materials. These sites are more prone to having local particle rearrangements, which can in turn further raise the structural anisotropy, forming a mechanism that leads to strain localization. During strain localization and failure, smaller particles can organize into larger rearrangements while keeping voids from growing, resulting in ductile behaviors. On the contrary, rearrangement in larger particles relies more on the highly underpacked sites, and a larger differential void growth was found for these particles, leading to brittle behaviors. Under this mechanism, the initially higher structural anisotropy for pillars with large particles works in favor of their brittleness, which could serve as a secondary effect that influences the brittle-to-ductile transition. This requires further investigation which decouples the initial structural anisotropy with particle interaction potentials.

The experimental method developed in this work is useful for studying the influences of particle-level features on local structures and dynamics as well as emergent system-scale behaviors such as the shear band formation, despite the relatively small system size. While this study demonstrates how the particle interaction range controls ductility as previous simulations predicted,[8,34–36] more mechanisms can also be tested using this apparatus. It is certainly possible to tune the capillary interaction more finely by adjusting particle/fluid density ratio, contact angle, surface tension, or even replace the liquid surface tension with a long-range elastic tension by covering particles with a thin elastic film.[73] We can also test the influence of surface friction,[26] deformability,[74] and particle shape[4] by using bubbles or 3D-printed particles. Including thermal noise by mechanically vibrating the liquid surface to study the effect of temperature and quenching[8,28] is also possible. These methods can be used for exploring, designing, and optimizing ductility and other mechanical properties of disordered materials.

Conflicts of interest

There are no conflicts to declare.

Acknowledgements

The authors would like to acknowledge the funding from the National Science Foundation grant MRSEC/DMR-1720530. We also thank Andrea J. Liu, Ge Zhang, and Robert A. Riggleman for helpful suggestions, as well as Douglas J. Jerolmack's group for the help with measuring particle sizes.

Notes and references

1 M. Chen, *Annu. Rev. Mater. Res.*, 2008, **38**, 445–469.
2 A. Greer, Y. Cheng and E. Ma, *Mater. Sci. Eng. R Rep.*, 2013, **74**, 71–132.
3 H. Lan, J. Chen and R. Macciotta, *Sci. Rep.*, 2019, **9**, 1–9.
4 L. Zhang, G. Feng, Z. Zeravcic, T. Brugarolas, A. J. Liu and D. Lee, *ACS nano*, 2013, **7**, 8043–8050.
5 M. L. Manning, J. S. Langer and J. Carlson, *Phys. Rev. E*, 2007, **76**, 056106.
6 A. Le Bouil, A. Amon, S. McNamara and J. Crassous, *Phys. Rev. Lett.*, 2014, **112**, 246001.
7 X. Ma and A. Elbanna, *Phys. Rev. E*, 2018, **98**, 022906.
8 E. Y. Lin and R. A. Riggleman, *Soft Matter*, 2019, **15**, 6589–6595.
9 R. J. Ivancic and R. A. Riggleman, *Soft Matter*, 2019, **15**, 4548–4561.
10 Y. Wang, K. Krishan and M. Dennin, *Phys. Rev. E*, 2006, **73**, 031401.
11 G. Katgert, M. E. Möbius and M. van Hecke, *Phys. Rev. Lett.*, 2008, **101**, 058301.

12 F. Tapia, D. Espíndola, E. Hamm and F. Melo, *Phys. Rev. E*, 2013, **87**, 014201.

13 P. Schall and M. van Hecke, *Annu. Rev. Fluid Mech.*, 2010, **42**, 67–88.

14 R. Kawamoto, E. Andò, G. Viggiani and J. E. Andrade, *J. Mech. Phys. Solids*, 2018, **111**, 375–392.

15 M. L. Falk and J. S. Langer, *Phys. Rev. E*, 1998, **57**, 7192.

16 A. Nicolas, E. E. Ferrero, K. Martens and J.-L. Barrat, *Rev. Mod. Phys.*, 2018, **90**, 045006.

17 E. D. Cubuk, R. Ivancic, S. S. Schoenholz, D. Strickland, A. Basu, Z. Davidson, J. Fontaine, J. L. Hor, Y.-R. Huang, Y. Jiang *et al.*, *Science*, 2017, **358**, 1033–1037.

18 V. Dansereau, V. Démery, E. Berthier, J. Weiss and L. Ponson, *Phys. Rev. Lett.*, 2019, **122**, 085501.

19 K. Karimi and J.-L. Barrat, *Sci. Rep.*, 2018, **8**, 1–10.

20 R. Dasgupta, H. G. E. Hentschel and I. Procaccia, *Phys. Rev. Lett.*, 2012, **109**, 255502.

21 M. L. Falk and J. S. Langer, *Annu. Rev. Condens. Matter Phys.*, 2011, **2**, 353–373.

22 P. Sollich, F. Lequeux, P. Hébraud and M. E. Cates, *Phys. Rev. Lett.*, 1997, **78**, 2020.

23 J. Lauridsen, M. Twardos and M. Dennin, *Phys. Rev. Lett.*, 2002, **89**, 098303.

24 M. Harrington and D. J. Durian, *Phys. Rev. E*, 2018, **97**, 012904.

25 C.-C. Kuo and M. Dennin, *J. Rheol.*, 2012, **56**, 527–541.

26 K. Karimi, D. Amitrano and J. Weiss, *Phys. Rev. E*, 2019, **100**, 012908.

27 X. Gu, S. J. Poon, G. J. Shiflet and J. Lewandowski, *Scr. Mater.*, 2009, **60**, 1027–1030.

28 M. Ozawa, L. Berthier, G. Biroli, A. Rosso and G. Tarjus, *Proc. Natl. Acad. Sci.*, 2018, **115**, 6656–6661.

29 H. Guo, P. Yan, Y. Wang, J. Tan, Z. Zhang, M. Sui and E. Ma, *Nature Mat.*, 2007, **6**, 735–739.

30 D. Sopu, A. Foroughi, M. Stoica and J. Eckert, *Nano Lett.*, 2016, **16**, 4467–4471.

31 H. J. Cho, N. B. Lu, M. P. Howard, R. A. Adams and S. S. Datta, *Soft Matter*, 2019, **15**, 4689–4702.

32 Y. Shi, *Appl. Phys. Lett.*, 2010, **96**, 121909.

33 S. Bonfanti, E. E. Ferrero, A. L. Sellerio, R. Guerra and S. Zapperi, *Nano Lett.*, 2018, **18**, 4100–4106.

34 M. Falk, *Physical Review B*, 1999, **60**, 7062.

35 O. Dauchot, S. Karmakar, I. Procaccia and J. Zylberg, *Phys. Rev. E*, 2011, **84**, 046105.

36 J. S. Babu, C. Mondal, S. Sengupta and S. Karmakar, *Soft Matter*, 2016, **12**, 1210–1218.

37 A. Schmeink, L. Goehring and A. Hemmerle, *Soft Matter*, 2017, **13**, 1040–1047.

38 A. Hemmerle, M. Schröter and L. Goehring, *Sci. Rep.*, 2016, **6**, 35650.

39 J. L. Hor, Y. Jiang, D. J. Ring, R. A. Riggleman, K. T. Turner and D. Lee, *ACS nano*, 2017, **11**, 3229–3236.

40 Y. Jiang, J. L. Hor, D. Lee and K. T. Turner, *ACS Appl. Mater. Interfaces*, 2018, **10**, 44011–44017.

41 M. Nicolson, Math. Proc. Camb. Philos. Soc., 1949, pp. 288–295.

42 P. A. Kralchevsky and K. Nagayama, *Adv. Colloid Interface Sci.*, 2000, **85**, 145–192.

43 P. Singh and D. Joseph, *J. Fluid Mech.*, 2005, **530**, 31–80.

44 M.-J. Dalbe, D. Cosic, M. Berhanu and A. Kudrolli, *Phys. Rev. E*, 2011, **83**, 051403.

45 I. Ho, G. Pucci and D. M. Harris, *Phys. Rev. Lett.*, 2019, **123**, 254502.

46 W. L. Bragg and J. Nye, *Proc. R. Soc. A*, 1947, **190**, 474–481.

47 D. Mazuyer, J. Georges and B. Cambou, *J. Phys.*, 1989, **50**, 1057–1067.

48 R. Kozlowski, C. M. Carlevaro, K. E. Daniels, L. Kondic, L. A. Pugnaloni, J. E. Socolar, H. Zheng and R. P. Behringer, *Phys. Rev. E*, 2019, **100**, 032905.

49 I. B. Liu, N. Sharifi-Mood and K. J. Stebe, *Annu. Rev. Condens. Matter Phys.*, 2018, **9**, 283–305.

50 N. Aubry, P. Singh, M. Janjua and S. Nudurupati, *Proc. Natl. Acad. Sci.*, 2008, **105**, 3711–3714.

51 H. Nishikawa, S. Maenosono, Y. Yamaguchi and T. Okubo, *J. Nanoparticle Res.*, 2003, **5**, 103–110.

52 B. F. Gibbs, S. Kermasha, I. Alli and C. N. Mulligan, *Int. J. Food Sci. Nutr.*, 1999, **50**, 213–224.

53 N. Tsapis, D. Bennett, B. Jackson, D. A. Weitz and D. Edwards, *Proc. Natl. Acad. Sci.*, 2002, **99**, 12001–12005.

54 M. Bandi, T. Tallinen and L. Mahadevan, *EPL*, 2011, **96**, 36008.

55 S. Knoche and J. Kierfeld, *Langmuir*, 2015, **31**, 5364–5376.

56 P. Cicuta and D. Vella, *Phys. Rev. Lett.*, 2009, **102**, 138302.

57 C. Planchette, E. Lorenceau and A.-L. Biance, *Soft Matter*, 2012, **8**, 2444–2451.

58 D. Vella, H.-Y. Kim, P. Aussillous and L. Mahadevan, *Phys. Rev. Lett.*, 2006, **96**, 178301.

59 J. M. Rieser, P. Arratia, A. Yodh, J. P. Gollub and D. Durian, *Langmuir*, 2015, **31**, 2421–2429.

60 M. Harrington, A. J. Liu and D. J. Durian, *Phys. Rev. E*, 2019, **99**, 022903.

61 J. M. Rieser, *Deformation of two-dimensional amorphous granular packings*, University of Pennsylvania, 2015.

62 M. Harrington, H. Xiao and D. J. Durian, *Granul. Matter*, 2020, **22**, 17.

63 W. He, N. Şenbil and A. Dinsmore, *Soft Matter*, 2015, **11**, 5087–5094.

64 R. Cook, *Concepts and Applications of Finite Element Analysis*, John Wiley and Sons, Inc., New York, 1974.

65 W. Li, J. M. Rieser, A. J. Liu, D. J. Durian and J. Li, *Phys. Rev. E*, 2015, **91**, 062212.

66 A. Le Bouil, A. Amon, J.-C. Sangleboeuf, H. Orain, P. Bésuelle, G. Viggiani, P. Chasle and J. Crassous, *Granular Matt.*, 2014, **16**, 1–8.

67 D. Turnbull and M. H. Cohen, *J. Chem. Phys.*, 1961, **34**, 120–125.

68 G. E. Schröder-Turk, W. Mickel, M. Schröter, G. W. Delaney,

M. Saadatfar, T. J. Senden, K. Mecke and T. Aste, *Europhys. Lett.*, 2010, **90**, 34001.

69 P. K. Morse and E. I. Corwin, *Phys. Rev. Lett.*, 2014, **112**, 115701.

70 Y. Cao, J. Li, B. Kou, C. Xia, Z. Li, R. Chen, H. Xie, T. Xiao, W. Kob, L. Hong *et al.*, *Nature Comm.*, 2018, **9**, 1–7.

71 E. D. Cubuk, S. S. Schoenholz, J. M. Rieser, B. D. Malone, J. Rottler, D. J. Durian, E. Kaxiras and A. J. Liu, *Phys. Rev. Lett.*, 2015, **114**, 108001.

72 J. M. Rieser, C. P. Goodrich, A. J. Liu and D. J. Durian, *Phys. Rev. Lett.*, 2016, **116**, 088001.

73 C. Lee, A. Buller and K. Dalnoki-Veress, *Bull. Am. Phys. Soc.*, 2020, **65**, P15.00008.

74 A. Boromand, A. Signoriello, J. Lowensohn, C. S. Orellana, E. R. Weeks, F. Ye, M. D. Shattuck and C. S. O'Hern, *Soft matter*, 2019, **15**, 5854–5865.

Tensile experiments of disordered granular particle rafts at an air-oil interface show that their ductility can be tuned by the particle size.